

A unified algorithm for the selection of collocation stencils for convex, concave, and singular problems

Thibault Jacquemin¹ | Stéphane P. A. Bordas^{1,2} 

¹Institute of Computational Engineering, University of Luxembourg, Esch-sur-Alzette, Luxembourg

²Institute of Research and Development, Duy Tan University, Danang, Viet Nam

Correspondence

Stéphane P. A. Bordas, Institute of Computational Engineering, University of Luxembourg, Maison du Nombre, 6 Avenue de la Fonte, L-4364 Esch-sur-Alzette, Luxembourg.
Email: stephane.bordas@alum.northwestern.edu

Funding information

European Union's Horizon 2020 research and innovation program, Grant/Award Number: 811099; Luxembourg National Research Fund, Grant/Award Number: INTER/FWO/15/10318764

Abstract

We introduce in this article a unified algorithm which allows the selection of collocation stencils, based on the visibility criterion, for convex, concave, and singular problems solved using a collocation method. The algorithm can be applied to any 2D or 3D problem. We show the importance of using a threshold angle, in conjunction with the visibility criterion, to assess of the inclusion of a node in the support of a collocation center. We also show how the algorithm can be used to assess the presence of a node in a defined domain. Such algorithm is particularly useful in the context of model refinement.

KEYWORDS

collocation method, concave domain, convex domain, generalized finite difference, model refinement, singular domain, stencil selection, support node selection, visibility criterion

1 | INTRODUCTION

The collocation methods constitute a family of computational methods initiated by Runge in 1908¹ with the finite difference method. These methods are used to approximate the solution of partial differential equation problems over defined domains. These methods can be applied to problems with smooth and non-smooth solution.² Many collocation methods have been proposed over the years. The most famous ones are the smooth particle hydrodynamics method (SPH),³ the reproduced kernel particle method (RKPM),⁴ the moving least squares method (MLS),⁵⁻⁷ and the generalized finite difference (GFD) method.⁸⁻¹³

The collocation methods use nodes placed on the boundary of the domain and in the domain to solve a set of partial differential equations. The field derivatives are approximated at each collocation center (or collocation node) as a function of the field values in the vicinity of the center. For this, a set of neighbor nodes, called support or stencil, is selected. The approximations of the field derivatives are based on these stencils.

The typical steps followed for solving a linear problem using a collocation method are as follows:

1. Determination of the collocation stencils;
2. Approximation the field derivatives based on the stencils;
3. Filling of the stiffness matrix and enforcement of the boundary conditions;
4. Solution of the linear problem;
5. Postprocessing of the results.

This is an open access article under the terms of the Creative Commons Attribution-NonCommercial-NoDerivs License, which permits use and distribution in any medium, provided the original work is properly cited, the use is non-commercial and no modifications or adaptations are made.

© 2021 The Authors. *International Journal for Numerical Methods in Engineering* published by John Wiley & Sons Ltd.

The determination of the collocation stencils is the first step. It is common to most collocation methods and key to ensure an optimum approximation of the field derivatives.²

The number of support nodes selected for each collocation node may depend on the location of the collocation node in the domain. It has been shown in Reference 2 that increasing the number of support nodes for collocation nodes on the boundary of the domain helps reducing significantly the observed error while maintaining the fill of the stiffness matrix reasonably low.

For singular problems, the visibility criterion, introduced as part of the element free Galerkin (EFG) method,¹⁴ has been proven effective for both meshless methods¹⁴⁻¹⁶ and collocation methods.^{2,17-19} The concept of the visibility criterion is presented in Figure 1(A). Considering a domain Ω , only the support nodes X_p which are “visible” from the collocation nodes X_c are considered in the stencil. In other words, the segments connecting X_c to the support nodes X_p shall not intersect the boundary of the domain. This can be understood by the fact that, in most collocation methods, the field derivatives at a collocation node are approximated as a function of the field values at the support nodes. For this, the solution needs to be continuous and as smooth as possible on the collocation stencil. In theory, only the nodes “visible” from the collocation nodes satisfy these criteria. We show in this article that an acceptance intersection angle can be beneficial for concave problems.

The diffraction criterion and the transparency criterion are other criteria, introduced in 1996 by Organ,²⁰ to select stencil nodes in the vicinity of a singularity. Both methods ensure a continuity of the weight functions at the singularity. In the context of fracture modeling based on the EFG method, it was showed that the visibility criterion was leading to spurious crack extensions unlike the diffraction or transparency criteria.²¹ The concept of the diffraction criterion is presented in Figure 1(B). The nodes X_p in the “hidden” zone are included in the stencil of a node X_c only if the distance between the collocation node and the singularity X_s plus the distance between the singularity and the candidate stencil node is lower than the selected stencil radius R_{sup} , that is, $\|X_s - X_c\| + \|X_p - X_s\| < R_{sup}$. The computation of the weight function is based on this extended distance. The transparency criterion is based on the same idea. The distance between a node X_c and a candidate stencil node X_p located in the “hidden” zone is increased by a function which depends on the distance between the singularity X_s and the point of intersection between the segment connecting the considered node to the candidate stencil node and a boundary of the domain.

The diffraction criterion and the transparency criterion have been used mostly in the context of fracture modeling using a weak form of the PDE. For a collocation method based on the GFD method, the use of the diffraction criterion did not lead to a lower error than the visibility criterion.² Also, the diffraction and transparency criteria cannot be readily applied to all type of convex problem. Therefore, the visibility criterion has been preferred in this work.

Methods such as intrinsic enrichment^{15,22,23} or extrinsic enrichment²⁴ have been used in the context of the EFG method to improve the accuracy of the solution in the vicinity of a crack tip using a known solution of the problem. A review of these methods and the computer implementation aspect is presented in Reference 16. Level sets have also

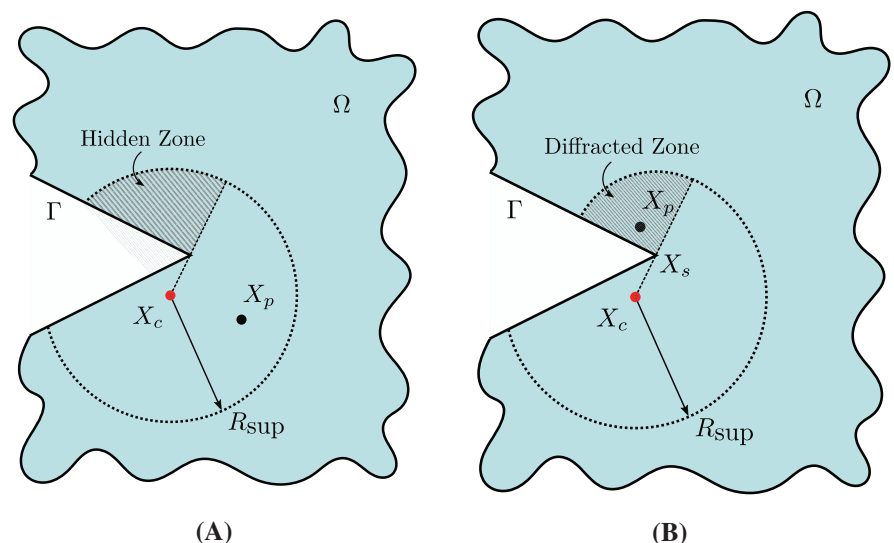


FIGURE 1 Concept of the visibility criterion (A) and of the diffraction criterion (B)

been used to model discontinuities and successfully applied to 3D problems by Rabczuk and Belytschko²⁵ or Zhuang et al.²⁶ The cracking particle methods is another method, proposed by Rabczuk and Belytschko,²⁷ to model cracks. This method uses a local enrichment of the test and trial functions at “cracked” particles to represent the discontinuity of the crack. The method has been proven robust in a number of papers.^{28,29} We focused in this work on a method applicable to all sort of problem and did not study in detail the specific case of crack propagation.

Some algorithms in the literature are commonly used to assess if a point is located in a polygon using the crossing number or the winding number methods described in References 30–32. Some other algorithms such as the Möller–Trumbore algorithm³³ or the AABB tree algorithm³⁴ are used to determine the number of intersections of a ray or segment with a triangulated surface. These algorithms can be used in the context of collocation to assess if a point of the segment connecting the collocation node to the support node is out of the domain. However, these methods do not provide flexibility with regards to the intersection tolerance between the domain boundary and the considered ray. Also, the computation cost can be reduced for the purpose of the visibility criterion as only a local definition of the concave areas of the domain is needed.

We propose in this article an algorithm which can be applied to any 2D or 3D problem (convex, concave, or singular) to allow the selection of support nodes based on the visibility criterion. We show the benefits of this algorithm in terms of error reduction for 2D and 3D concave linear elastic problems using the GFD method. We also assess how the selection of a threshold angle, as part of the visibility criterion, impacts the solution of collocation problems. To the authors’ knowledge, a detailed description of the node selection algorithm, considering a specified threshold angle in the implementation of the visibility criterion, is not present in the literature.

The proposed algorithm is presented in Section 2. Some results are presented in Section 3 for 2D and 3D problems for which an analytical solution is known. We show in this section the importance of the selected threshold angle. Finally, we show in Section 4 how the algorithm can be used in the context of model refinement. The code and all data files used to generate the results presented are attached to this article to facilitate further developments of the proposed method.

2 | ALGORITHM

The node selection algorithm is split into multiple sub-algorithms: the general node selection algorithm is presented in Section 2.1 and the specific details of the algorithm for concave domains in Section 2.2. The algorithms are presented in the form of flow charts and pseudo codes.

2.1 | Support node selection algorithm

Several methods can be considered to select the nodes to be included in the stencil of a collocation node. Schönauer³⁵ proposed a method based on the selection of rings of nodes around the collocation node. Kennett et al.³⁶ introduced a selection method for anisotropic point distributions. Seibold presented a method to ensure that the selected nodes lead to a positive stencil.³⁷ Davydov proposed an algorithm to select the support nodes based on the angles formed by the collocation node and two adjacent support nodes for 2D problems³⁸ and another algorithm based on the 8-octant criterion³⁹ for 3D problems. Even though many methods have been proposed, the most commonly used methods remain the distance criterion¹⁰ and the quadran criterion introduced by Liszka and Orkisz.¹²

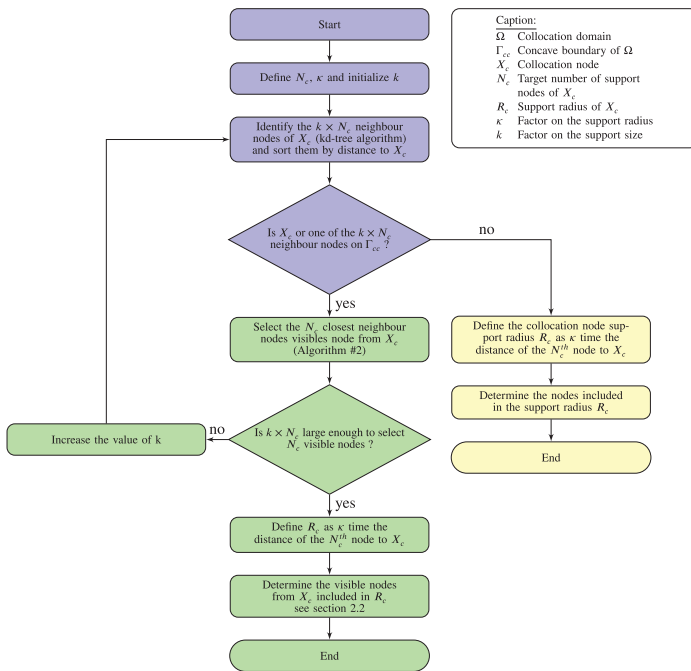
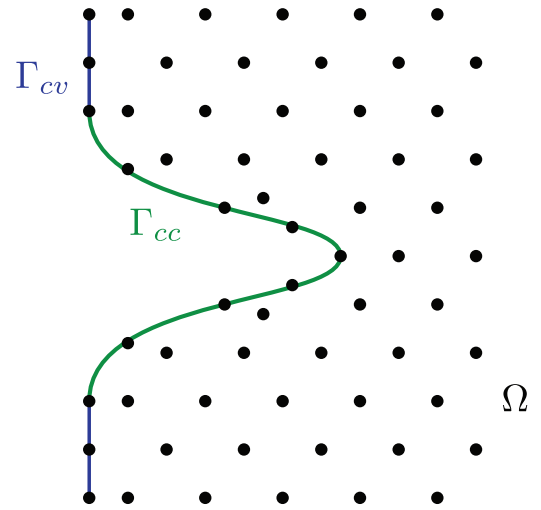
A domain Ω , limited by the boundary Γ , is considered. The boundary of the domain is split into a concave boundary Γ_{cc} and a convex boundary Γ_{cv} (see Figure 2). The nodes X_p to be included in the support of each collocation nodes X_c can be identified using the algorithm presented in Figure 3(A).

We considered the distance criterion in our work but the algorithm can also be used to determine the candidate nodes for other node selection methods.

2.2 | Algorithm

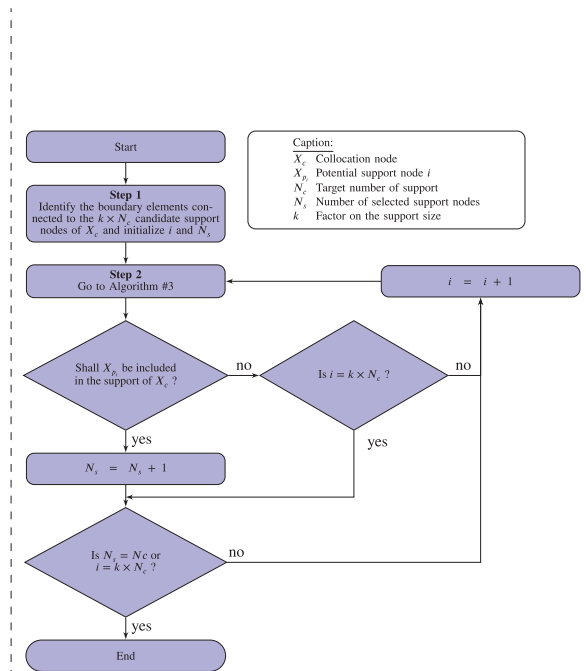
We present in this section the node selection algorithm.

FIGURE 2 Concave domain Ω , defined by the boundaries Γ_{cv} and Γ_{cc}



Algorithm #1 flowchart for collocation support node selection. The central branch of the flowchart, in green, is the path followed for the collocations nodes near a concave boundary of the domain, if any. The right branch is the path for the nodes far from a concave boundary of the domain.

(A)



Algorithm #2 flowchart for support node selection near a concave boundary of the domain.

(B)

FIGURE 3 Algorithm #1 (left) and Algorithm #2 (right)

The number of support nodes N_c to be considered in the stencil of a collocation node X_c is selected based on the position of the collocation node in the domain (e.g., on the boundary of the domain or inside of the domain) and based on the regularity of the node placement. All the N_c time k nodes in the vicinity of X_c , which could be included in the support are considered as candidate nodes for the stencil. k is larger than 1.0 as some nodes might not be included in the support of the collocation node if they are not “visible” from X_c or if some nodes are located at the same distance from the collocation node. κ is a factor used to scale the support radius once the target number of support nodes has been identified. This allows the selection of all the nodes located at a distance R_c from X_c .

The algorithm allowing the selection of the support nodes near a concave boundary of the domain are presented in Figure 3(B). More details about the steps 1–4 are provided below.

Step 1: Details

In order to assess if a node is “visible” from a collocation node, the concave boundaries of the domain need to be known. Even if the collocation methods do not make use of elements to solve the partial differential equation problem, the use of boundary elements, in the concave regions of the domain, is a simple and efficient method to enforce the visibility criterion. Figure 4 shows a concave domain Ω . The concave boundary of the domain, Γ_{cc} , is discretized using boundary elements. The outer normals to the boundary elements are then calculated. These normals allow positioning the inside of the domain relatively to the boundary and are used to assess if the segment connecting a collocation node to a support node interests the boundary. In case of an intersection, the angle between the segment and the crossed element can be calculated.

Step 2: Details

In this step, the inclusion of each candidate support node is assessed using the visibility criterion based on Algorithm #3 presented in Figure 5.

Step 3: Details

Step 3 involves three sub-steps which are described below.

(a) Compute the parameters of the intersection between the segment connecting X_c to X_{p_i} and the considered boundary element. The coordinates of the intersection point can be calculated as a function of X_c , X_{p_i} and of the element corner nodes (X_1 , X_2 , and X_3 in Figure 6). For instance, for the 2D and 3D cases presented in Figure 6, the coordinates of the intersection points are calculated by solving the systems presented in Equations (1) and (2) for the 2D and 3D cases, respectively.

$$\begin{bmatrix} x_c - x_{p_i} & x_2 - x_1 \\ y_c - y_{p_i} & y_2 - y_1 \end{bmatrix} \begin{bmatrix} \alpha \\ \beta \end{bmatrix} = \begin{bmatrix} x_c - x_1 \\ y_c - y_1 \end{bmatrix}, \quad (1)$$

$$\begin{bmatrix} x_c - x_{p_i} & x_2 - x_1 & x_3 - x_1 \\ y_c - y_{p_i} & y_2 - y_1 & y_3 - y_1 \\ z_c - z_{p_i} & z_2 - z_1 & z_3 - z_1 \end{bmatrix} \begin{bmatrix} \alpha \\ \beta \\ \gamma \end{bmatrix} = \begin{bmatrix} x_c - x_1 \\ y_c - y_1 \\ z_c - z_1 \end{bmatrix}. \quad (2)$$

(b) Compute the scalar product of the vector $\mathbf{X}_{cp_i} = \frac{X_{p_i} - X_c}{\|X_{p_i} - X_c\|}$ with the normal \mathbf{n}_j of the identified boundary elements.

(c) Define a threshold ϵ , based on an acceptable intersection angle between the boundary element and the segment connecting the collocation node to the support node. ϵ is expressed as a function of a threshold angle θ corresponding to the angle between the element and the vector \mathbf{X}_{cp_i} . We have $\epsilon = \cos\left(\frac{\pi}{2} - \theta\right)$.

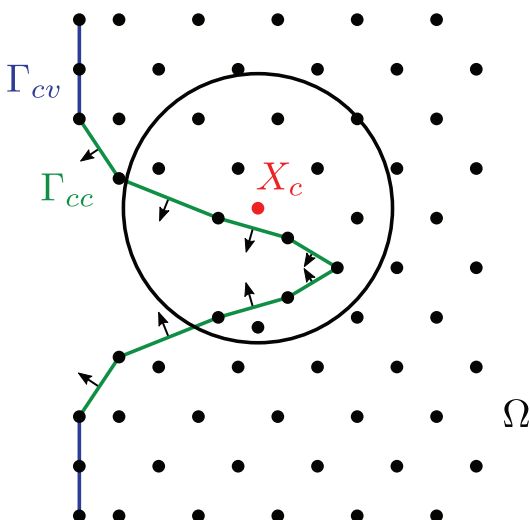
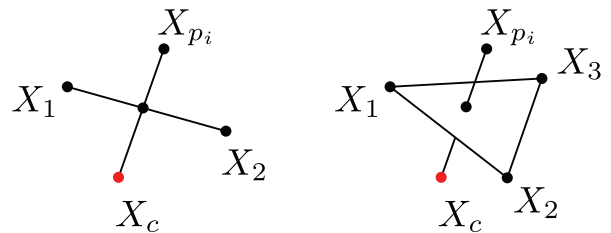


FIGURE 4 The concave boundaries of the domain are discretized by elements and the outer normal of each element is calculated

<p>Algorithm #3</p> <p>For each concave boundary element identified in Step 1</p> <p>Go to Step 3.</p> <p>Case: 2D problem</p> <p>if ($0 < \alpha < 1$ and $0 < \beta < 1$ and $\text{abs}(\mathbf{n}_j \cdot \mathbf{X}_{cp_i}) > \epsilon$)</p> <p>Do not include X_{p_i} in the support of X_c. Exit from the loop.</p> <p>else if ($(\alpha = 0$ or $\alpha = 1)$ and $0 \leq \beta \leq 1$)</p> <p>Go to Step 4.</p> <p>else if ($(\beta = 0$ or $\beta = 1)$ and $0 \leq \alpha \leq 1$)</p> <p>Go to Step 4.</p> <p>Case: 3D problem</p> <p>if ($0 < \alpha < 1$ and $0 < \beta < 1$ and $0 < \gamma < 1$ and $\beta + \gamma < 1$ and $\text{abs}(\mathbf{n}_j \cdot \mathbf{X}_{cp_i}) > \epsilon$)</p> <p>Do not include X_{p_i} in the support of X_c. Exit from the loop.</p> <p>else if ($(\alpha = 0$ or $\alpha = 1)$ and $0 \leq \beta \leq 1$ and $0 \leq \gamma \leq 1$ and $\beta + \gamma \leq 1$)</p> <p>Go to Step 4.</p> <p>else if ($(\beta = 0$ or $\beta = 1)$ and $0 \leq \alpha \leq 1$ and $0 \leq \gamma \leq 1$ and $\beta + \gamma \leq 1$)</p> <p>Go to Step 4.</p> <p>else if ($(\gamma = 0$ or $\gamma = 1)$ and $0 \leq \alpha \leq 1$ and $0 \leq \beta \leq 1$ and $\beta + \gamma \leq 1$)</p> <p>Go to Step 4.</p> <p>end</p>
--

FIGURE 5 Algorithm #3 for the cases of 2D and 3D problems

FIGURE 6 Intersection of a segment connection a collocation node X_c and a neighbor node X_{p_i} with a boundary element for the 2D (left) and the 3D (right) cases



<p>Algorithm #4</p> <p>Initialize Count1, Count2 and n to zero.</p> <p>For each boundary element j connected to the point of intersection</p> <p>$n = n + 1$</p> <p>if ($\alpha < 0.5$ and $\mathbf{n}_j \cdot \mathbf{X}_{cp_i} > \epsilon$)</p> <p>Count1 = Count1 + 1</p> <p>else if ($\alpha \geq 0.5$ and $\mathbf{n}_j \cdot \mathbf{X}_{cp_i} < -\epsilon$)</p> <p>Count2 = Count2 + 1</p> <p>end</p> <p>if (Count1 = n or Count2 = n)</p> <p>Do not include X_{p_i} in the support of X_c.</p>
--

FIGURE 7 Algorithm #4 for the cases of 2D and 3D problems

Step 4: Details

Identify the elements connected to the point of intersection between the segment connecting X_c to X_{p_i} and the considered element. Use Algorithm #4 presented in Figure 7 to assess if the node X_{p_i} shall be included in the support of X_c .

3 | RESULTS

3.1 | General

We presented in Section 2 an algorithm allowing the selection of support nodes for collocation problems. We show in this section the benefits of using the algorithm for 2D and 3D problems and the benefits of using a threshold

angle in conjunction with the visibility criterion. Problems with an analytical solution have been selected for this purpose. The impact of the proposed algorithm on the observed error can therefore be assessed. We first present the governing equations of linear elasticity and the error norm considered before presenting results for 2D and 3D problems.

3.2 | Governing equations

The 2D and 3D problems considered in this work are linear elastic problems. The partial differential equations associated to this class of problems are presented in this section for the general case of 3D problems.

The equilibrium of a solid Ω subject to body forces \mathbf{b} is expressed as a function of the stress tensor $\boldsymbol{\sigma}$ by the Newton's second law. For static problems, the equilibrium equation is

$$\begin{aligned} \nabla \boldsymbol{\sigma} + \mathbf{b} &= \mathbf{0}, \\ \text{or } \sigma_{ij,j} + b_i &= 0. \end{aligned} \quad (3)$$

The equilibrium equation is expressed as a function of the displacement field \mathbf{u} at each node of the domain using:

- the relationship between the displacement field and the strain field $\boldsymbol{\epsilon}$

$$\begin{aligned} \boldsymbol{\epsilon} &= \frac{1}{2} (\nabla \mathbf{u} \nabla \mathbf{u}^T) \\ \text{or } \epsilon_{ij} &= \frac{1}{2} (u_{i,j} + u_{j,i}), \end{aligned} \quad (4)$$

- the Hook's law which gives the relationship between the strain field and the stress field (presented here in the Voigt form):

$$\begin{bmatrix} \sigma_{11} \\ \sigma_{22} \\ \sigma_{33} \\ \sigma_{23} \\ \sigma_{13} \\ \sigma_{12} \end{bmatrix} = \frac{E}{(1+\nu)(1-2\nu)} \begin{bmatrix} 1-\nu & \nu & \nu & 0 & 0 & 0 \\ \nu & 1-\nu & \nu & 0 & 0 & 0 \\ \nu & \nu & 1-\nu & 0 & 0 & 0 \\ 0 & 0 & 0 & 1-2\nu & 0 & 0 \\ 0 & 0 & 0 & 0 & 1-2\nu & 0 \\ 0 & 0 & 0 & 0 & 0 & 1-2\nu \end{bmatrix} \begin{bmatrix} \epsilon_{11} \\ \epsilon_{22} \\ \epsilon_{33} \\ \epsilon_{23} \\ \epsilon_{13} \\ \epsilon_{12} \end{bmatrix}. \quad (5)$$

The above equations can easily be used for 2D problems using either the plane stress assumption (i.e., $\sigma_{33} = 0$) or the plane strain assumption (i.e., $\epsilon_{33} = 0$).

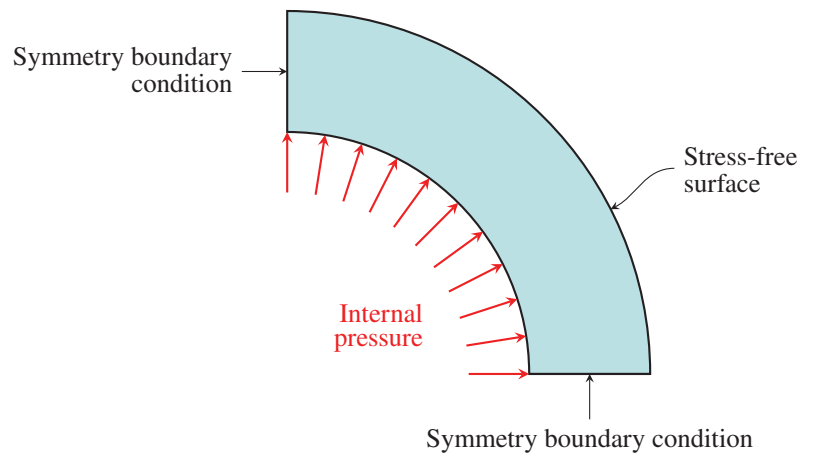
Dirichlet and Neumann boundary conditions are, respectively, applied to the degrees of freedom of the collocation nodes located on the boundaries Γ_D and Γ_N . The known displacement field \mathbf{u}^e is applied on Γ_D . An external force \mathbf{f}^e is applied to the nodes located on Γ_N . The outer normal \mathbf{n}_N allows the computation of the pressure at the nodes of Γ_N . Dirichlet and Neumann boundary conditions can be applied to different degrees of freedom of the same node.

$$\begin{aligned} \mathbf{u} &= \mathbf{u}^e && \text{on } \Gamma_D, \\ \boldsymbol{\sigma} \mathbf{n}_N &= \mathbf{f}^e \quad \text{or} \quad \sigma_{ij} n_j = f_i^e && \text{on } \Gamma_N. \end{aligned} \quad (6)$$

3.3 | Error norm

The error considered here is the L_2 relative error norm (noted L_2R). At a collocation node \mathbf{X}_k , the exact stress and approximated stress solutions are noted $\sigma_{ij}^e(\mathbf{X}_k)$ and $\sigma_{ij}^h(\mathbf{X}_k)$, respectively. Considering a domain Ω discretized by n collocation

FIGURE 8 2D model of pressurized cylinder. Symmetric boundary conditions are applied to the vertical and horizontal edges of the domain. A constant pressure loading is applied to the inner surface of the cylinder. A stress-free surface boundary condition is applied to the outer surface



nodes, the L_2 relative error norm is calculated as per Equation (7)

$$L_2R(\sigma_{ij}) = \frac{\sqrt{\sum_{k=1}^n (\sigma_{ij}^e(\mathbf{X}_k) - \sigma_{ij}^h(\mathbf{X}_k))^2}}{\sqrt{\sum_{k=1}^n \sigma_{ij}^e(\mathbf{X}_k)^2}}. \quad (7)$$

In this article, the GFD method is used to solve the problems considered.

3.4 | 2D problems

3.4.1 | Problems considered

We consider three concave problems in 2D: one with a concavity of low curvature, another one with a concavity of high curvature, and a singular problem. The problems considered are

- a cylinder under internal pressure;
- an infinite plate with an elliptical hole under biaxial loading;
- a L-shape domain in mode I loading.

We used Gmsh⁴⁰ to generate uniform node distributions in the considered domains. The discretizations are attached with this article.

2D cylinder

The model of the 2D cylinder is presented in Figure 8. Due to the symmetries of the problem in the Cartesian coordinate system, only a quarter of the cylinder is modeled. Symmetric boundary conditions are applied to the vertical edge on the left of the domain and to the horizontal edge at the bottom of the domain. An internal pressure loading is applied to the inner surface of the cylinder. Stress-free surface boundary conditions are applied to the outer surface. The well-known solution of this problem is presented in Figure 9 for the stress components σ_{11} , σ_{12} , and σ_{22} and for the von Mises stress σ_{VM} .

Infinite plate with an elliptical hole

The second problem considered is an infinite plate with an elliptical hole under biaxial loading (see Figure 10). Symmetric boundary conditions are applied to the nodes on the vertical edge on the left of the model and stress-free surface boundary conditions are applied to elliptical hole. The displacement field of the exact solution is applied to the other boundaries of the domain. The solution to this problem is presented by Gao.⁴¹ We show the solution for the stress components σ_{11} , σ_{12} , and σ_{22} and for the von Mises stress σ_{VM} in Figure 11.

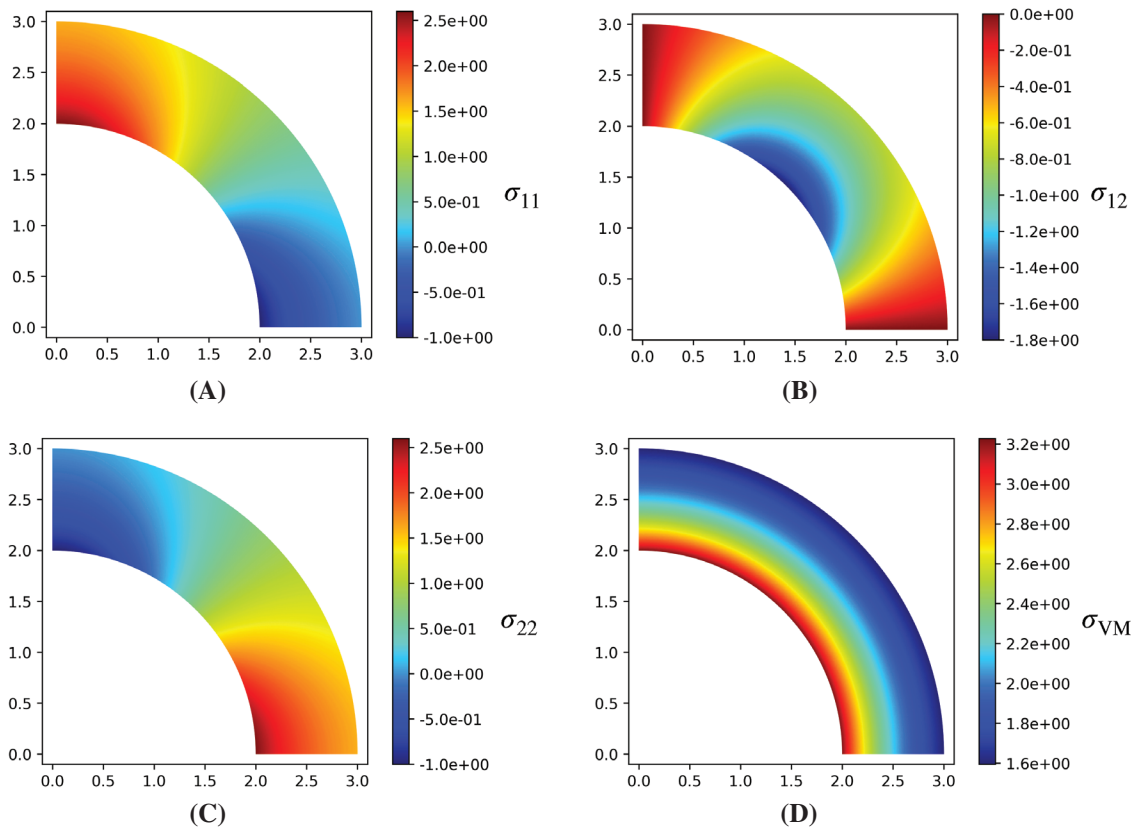


FIGURE 9 Exact stress solution of a pressurized cylinder. Only a quarter of the cylinder is considered due to the symmetries of the domain in the Cartesian coordinate system

L-shape

The model of a 2D L-shape domain is presented in Figure 12. Stress-free boundary conditions are applied to the inner surface of the “L.” The displacement field of the exact solution is applied to the other boundaries of the domain. The solution to this problem is presented by Babuška and Suri⁴² and by Ainsworth and Senior.⁴³ We show the solution for the stress components σ_{11} , σ_{12} , and σ_{22} and for the von Mises stress σ_{VM} in Figure 13.

3.4.2 | Results

We analyze in this section the impact of the visibility criterion, based on the algorithm presented in Section 2, for different threshold angles θ . The results for the 2D cylinder, for the infinite plate with an elliptical hole, and for the L-shape domain are, respectively, presented in Figures 14–16.

We can see from the results presented in Figure 14, for the 2D cylinder, that the visibility criterion leads to an increase of the observed error in terms of L_2 relative norm when a threshold angle of 0.0° is used. With a threshold angle of 1.0° and 5.0° , the observed error is very close to the reference case where the visibility criterion is not considered.

When a threshold angle of 0.0° is selected, the nodes on the concave boundary of the domain are excluded from the stencils of the collocation nodes also located on a concave boundary of the domain. The results show that, for a model having a concavity of low curvature such as the 2D cylinder, the inclusion of these nodes in the stencils (when a threshold angle of 1.0° or 5.0° is selected) leads to a lower error than the exclusion of these nodes.

The results presented in Figure 15, for the infinite plate with an elliptical hole, show that the use of the visibility criterion almost always leads to a reduction of the observed error compared to the reference case where the visibility criterion is not considered. With a threshold angle of 0.0° , the error reduction is not constant. For most node discretizations, the

FIGURE 10 2D model of an infinite plate with an elliptical hole under biaxial loading. Symmetric boundary conditions are applied to the vertical edge on the left. Stress-free surface boundary conditions are applied to the boundary of the elliptical hole. The displacement field of the exact solution is applied to the other boundaries of the domain

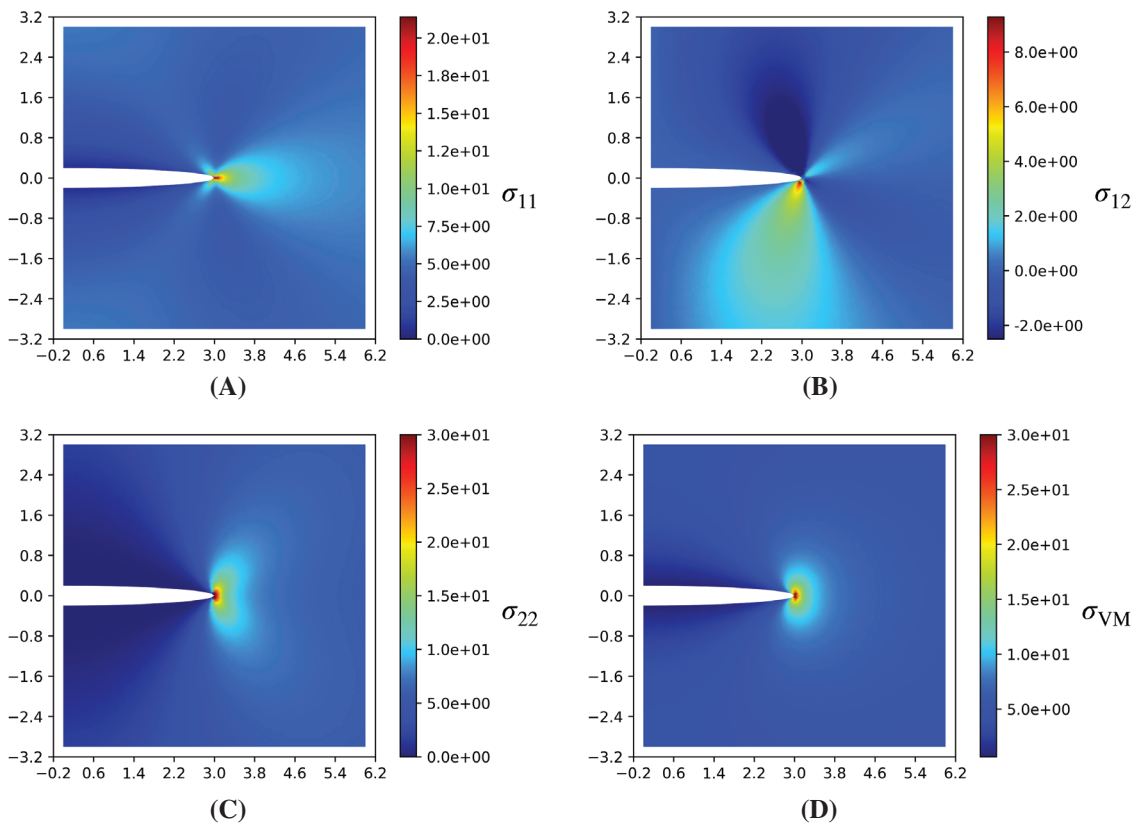
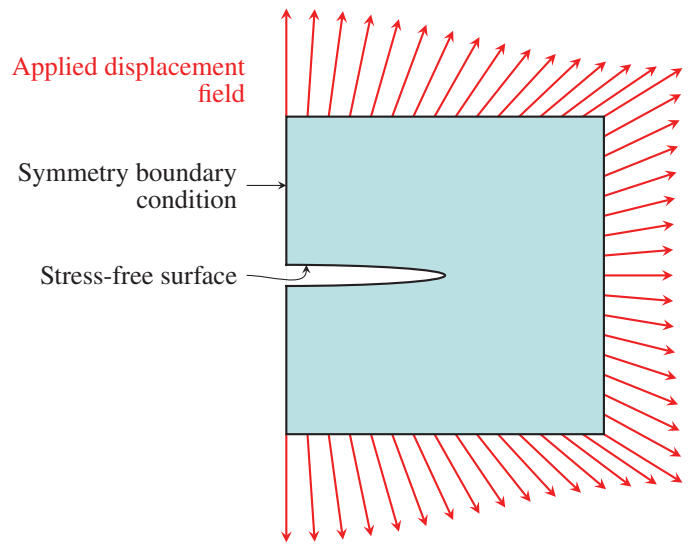


FIGURE 11 Exact stress solution of an infinite plate with an elliptical hole under biaxial loading. For the subfigures (C) and (D), the maximum stress is at the point of largest curvature. In order to present the stress results over the domain, we truncated the stress solution with a defined threshold. The stress solutions larger than this threshold are shown in the same color as the selected threshold values

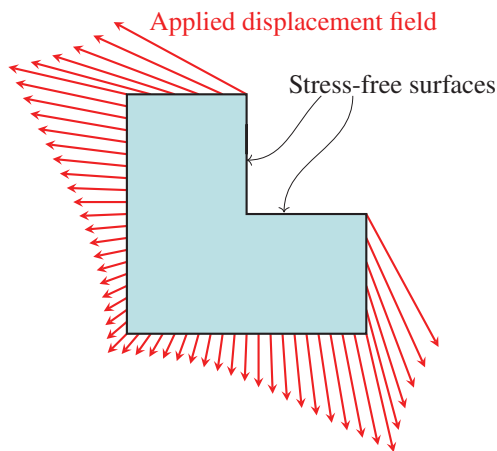


FIGURE 12 2D model of L-shape domain in mode I loading. Stress-free surface boundary conditions are applied to the inner surface of the “L.” The displacement field of the exact solution is applied to the other boundaries of the domain

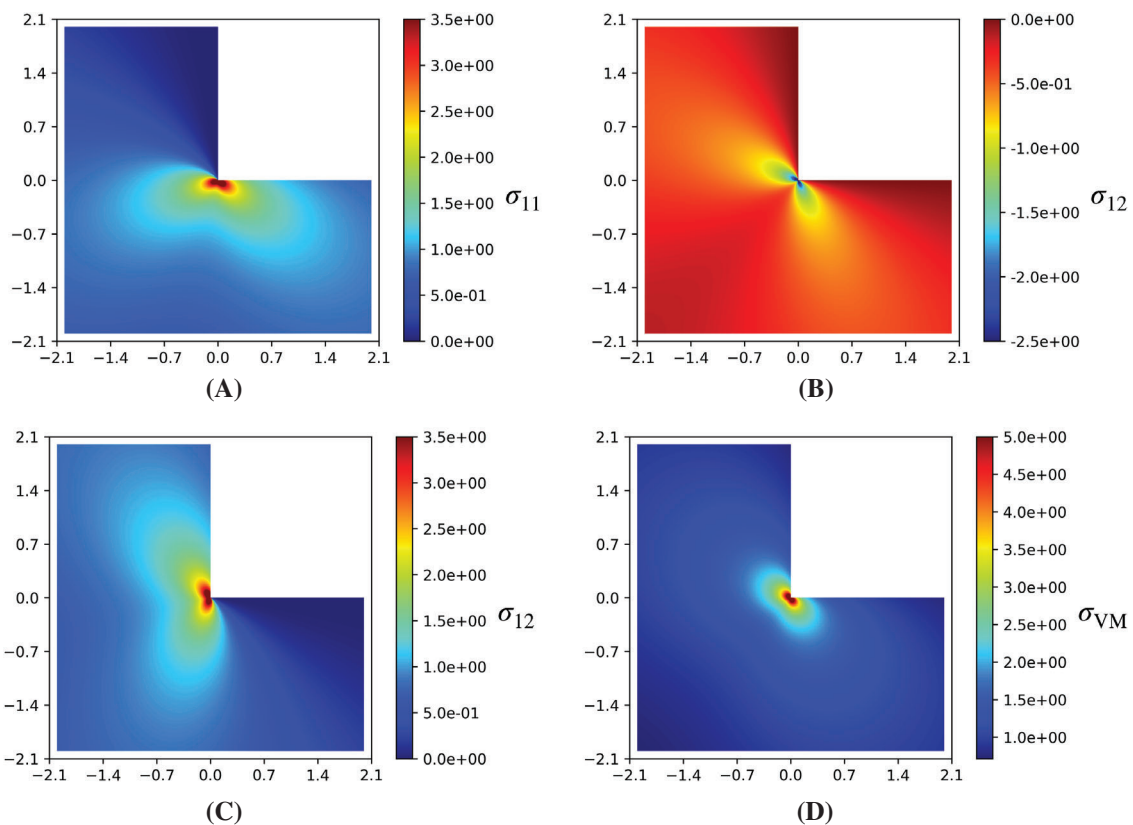


FIGURE 13 Exact stress solution of a L-shape domain in mode I loading. In order to present the stress results over the domain, we truncated the stress solution with a defined threshold. The stress solutions larger than this threshold are shown in the same color as the selected threshold values

results obtained with threshold angles of 1.0° and 5.0° lead to the smallest error. An error reduction is observed for the relatively coarse discretizations when a threshold angle of 40° is selected. No error reduction is observed for the finer discretizations for such threshold angle.

The exclusion of some nodes from the stencil of collocation nodes located near concave boundaries of the domain allows capturing more precisely the geometry of the domain, especially in the areas having a concavity of high curvature. The fact that a threshold angle of 0.0° leads to a higher error than a threshold angle of 1.0° or 5.0° shows that the inclusion of some boundary nodes in the areas having a concavity of low curvature allows a reduction of the error, as for the 2D cylinder problem. As expected, the selection of a large threshold

FIGURE 14 Comparison of the error between a case without consideration of the visibility criterion and cases with consideration of the visibility criterion for different threshold angles for the 2D pressurized cylinder problem. The error in terms of L_2 relative norm is presented for the σ_{11} , σ_{12} , and σ_{22} stress components and for the von Mises stress noted σ_{VM}

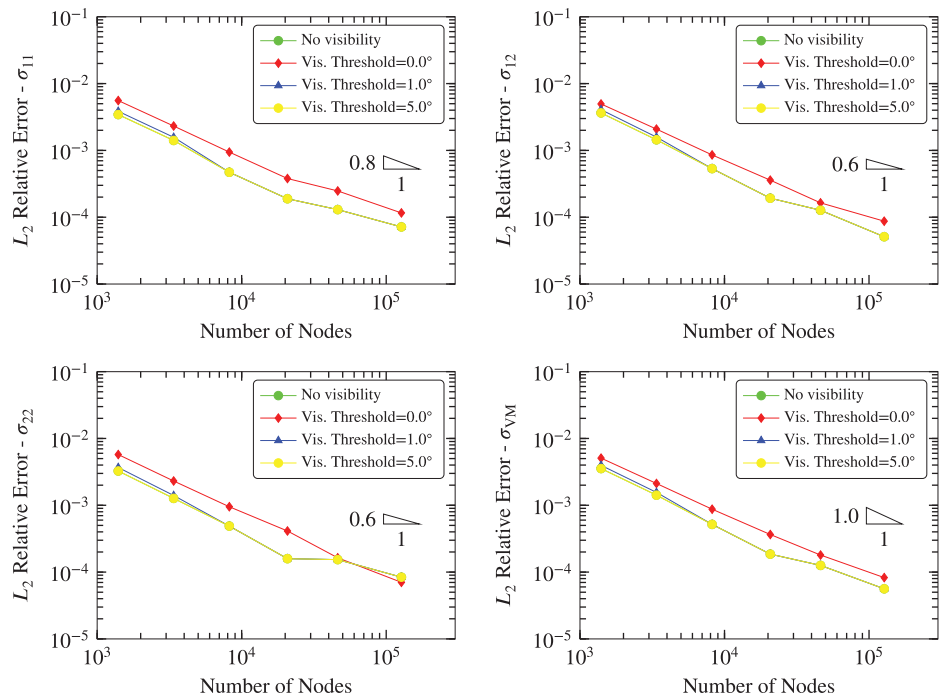
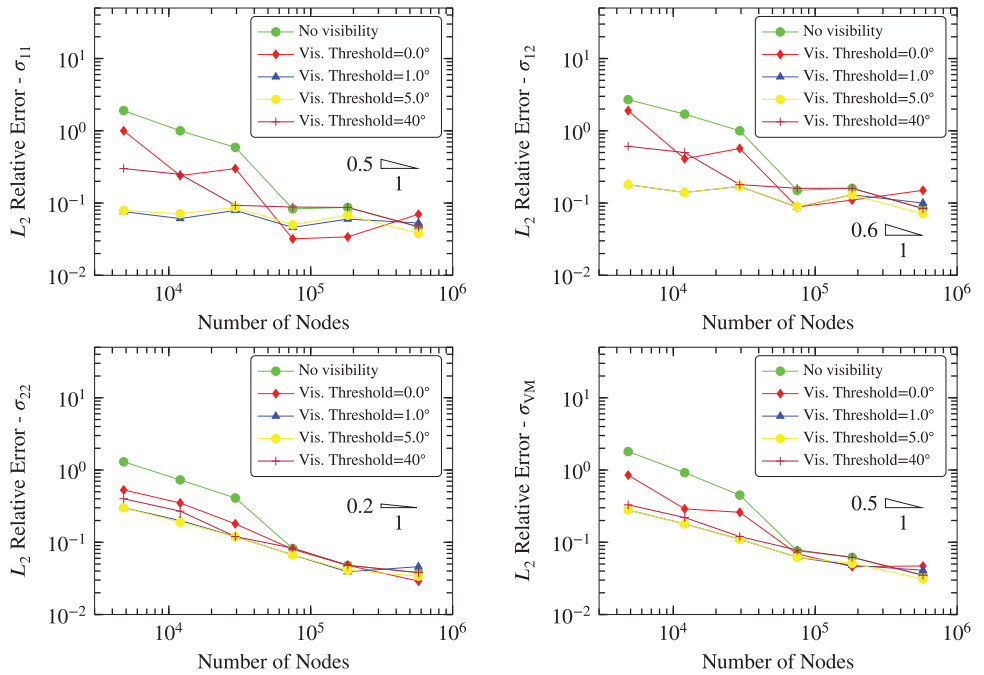


FIGURE 15 Comparison of the error with and without consideration of the visibility criterion for an infinite plate with an elliptical hole under biaxial loading. The error in terms of L_2 relative norm is presented for the σ_{11} , σ_{12} , and σ_{22} stress components and for the von Mises stress noted σ_{VM}



angle of 40° leads to a higher error than with a smaller threshold angle. The concave boundary of the domain is less accurately captured since some segments connecting collocation nodes to support nodes intersect the boundary of the domain. The observed error remains below the error for the model where the visibility criterion is not considered.

The results presented in Figure 16, for the L-shape problem, show that the use of the visibility criterion leads to a significant error reduction compared to the reference case where the visibility criterion is not considered. For this problem, the selected threshold angle does not impact the results. This result is expected since a threshold angle in the order of 0° – 5° has little impact on the selection of the support nodes in the singular region since the angle of the boundary at the singularity is of 90° .

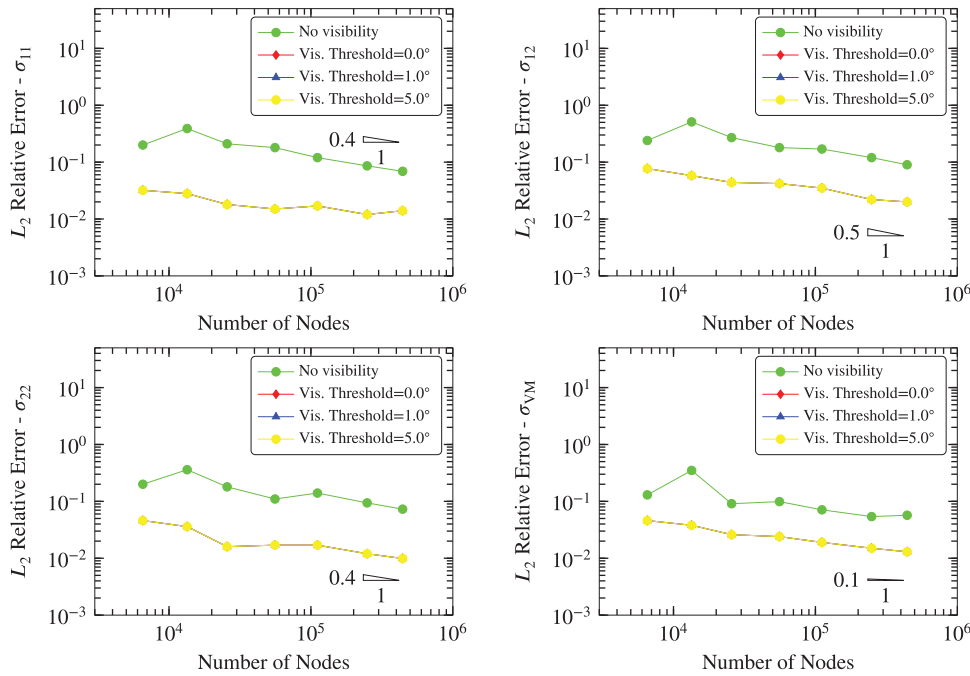


FIGURE 16 Comparison of the error with and without consideration of the visibility criterion for a L-shape domain in mode I loading. The error in terms of L_2 relative norm is presented for the σ_{11} , σ_{12} , and σ_{22} stress components and for the von Mises stress noted σ_{VM} . The observed error is the same for the visibility thresholds considered

The results presented in Figure 14 differ from the results presented in Figures 15 and 16 since, for the 2D cylinder, the consideration of the visibility criterion with a threshold angle of 0.0° leads to an increase of the error. This can be explained by the smoothness of the solution for this problem, even in the concave region. We observe that, for this problem, the inclusion of adjacent boundary nodes in the stencil of collocation nodes located on the concave boundary improves the approximation of the PDE at this node.

We showed in this section that the visibility criterion can be applied to concave problems with high and low curvatures and to singular problems. The selection of a threshold angle is important to ensure that, for all problems, the use of the visibility criterion leads to an error reduction or does not lead to an increase of the error. In this work, we select a threshold angle of 5.0° as it leads to the lowest error for the 2D cylinder problem. Such a threshold angle leads to a significant error reduction compared to the reference case for the problem of an infinite plate with an elliptical hole for most discretizations.

3.5 | 3D problems

3.5.1 | Problems considered

Three 3D problems for which analytical solutions are known are considered in this section. These problems are the 3D extensions of the problems considered in 2D:

1. an infinite body with a spherical cavity under remote stress loading;
2. an infinite 3D plate with an elliptical hole under biaxial loading;
3. a 3D L-shape in mode I loading.

As for the 2D problems, we generated uniform node distributions in the considered domains using Gmsh.⁴⁰ The discretizations are attached with this article.

The first problem has a concavity of low curvature, the second, a concavity of high curvature and the last one, a singularity. For each problem, we show a comparison in terms of L_2 relative error norm of the results from models without and with consideration of the visibility criterion in the collocation stencil selection. A threshold angle of 5.0° is considered for the models with the visibility criterion (based on the results presented in the previous section). The comparison is performed for a coarse and a fine model.

Infinite body with a spherical cavity

The model of an infinite body with a spherical cavity is presented in Figure 17. The infinite body is subject to a uniform stress loading $\sigma_{33} = \sigma_0$ far from the cavity. The solution to this problem is presented in a number of papers^{44,45} and is shown in Figure 18.

The L_2 relative error norm is presented for the σ_{11} , σ_{12} , σ_{13} , σ_{33} , and σ_{VM} stress components in Table 1. The results for the stress components σ_{22} and σ_{23} are not presented due the symmetries of the problem.

Infinite 3D plate with an elliptical hole

The model of a 3D infinite plate with an elliptical hole under biaxial loading is presented in Figure 19. The solution to this problem is presented in Section 3.4.1 for the 2D case. Symmetric boundary conditions are applied to plane YZ. Stress-free surface boundary conditions are applied to the boundary of the elliptical hole and to the top surface of the plate. The bottom surface of the plate is fixed in the Z direction. The displacement field of the exact solution is applied to the other boundaries of the domain.

The L_2 relative error norm is presented in Table 2 for the σ_{11} , σ_{12} , and σ_{22} stress components and for the von Mises stress σ_{VM} . The results for the stress components σ_{13} , σ_{23} , and σ_{33} are not presented as the stresses are null for these components.

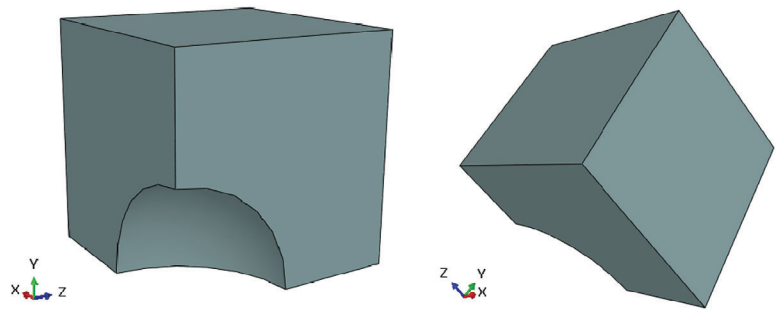


FIGURE 17 Infinite body with a spherical cavity under remote stress loading. Symmetric boundary conditions are applied to the symmetry planes XY, XZ, and YZ. Stress-free surface boundary conditions are applied to the internal surface of the spherical cavity. The displacement field of the exact solution is applied to the other boundaries of the domain

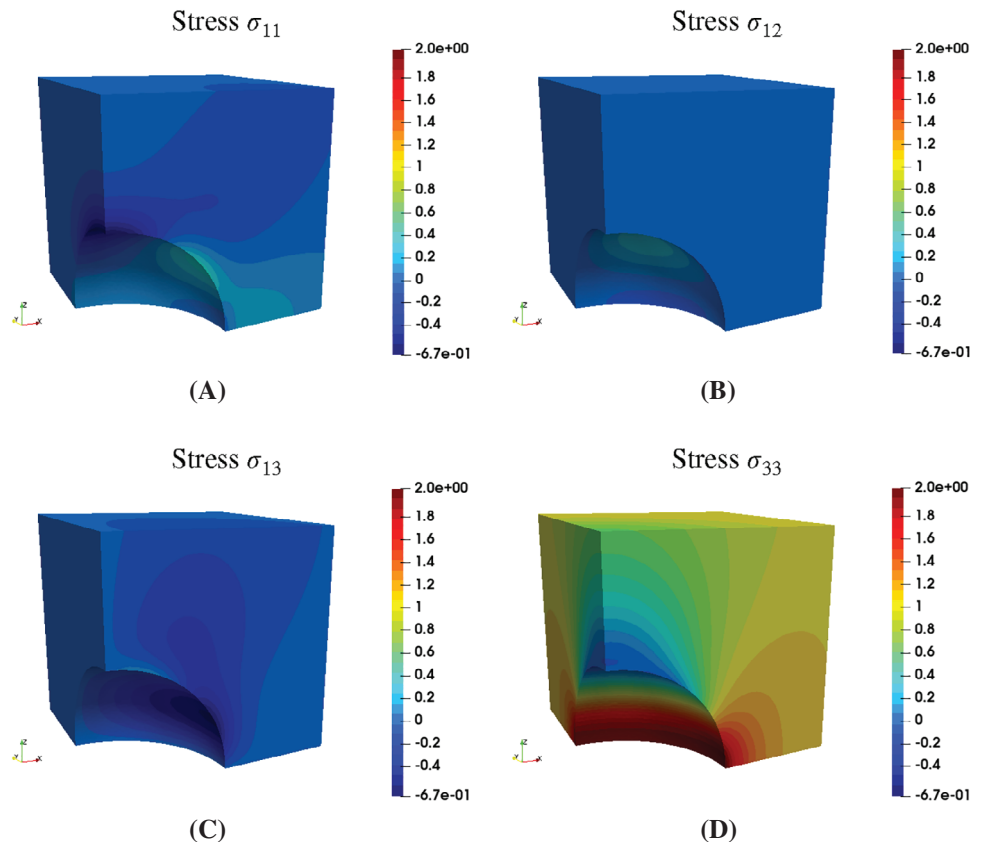
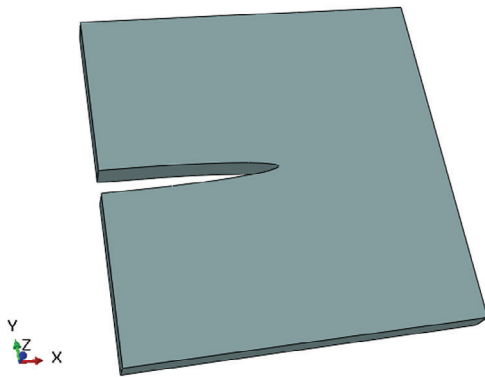


FIGURE 18 Exact stress solution of an infinite body with a spherical cavity under remote loading ($\sigma_{33} = \sigma_0$ far from the cavity)

TABLE 1 Results in terms of L_2 relative error norm for the problem of an infinite body with a spherical cavity

Parameter	Coarse model (45,251 nodes)		Fine model (183,281 nodes)	
	w/o visibility criterion	w/ visibility criterion	w/o visibility criterion	w/ visibility criterion
σ_{11}	1.200E-01	1.134E-01	3.583E-02	3.453E-02
σ_{12}	1.171E-01	1.015E-01	3.544E-02	3.421E-02
σ_{13}	5.877E-02	5.964E-02	2.387E-02	2.378E-02
σ_{33}	1.088E-02	9.885E-03	3.851E-03	3.663E-03
σ_{VM}	1.116E-02	9.948E-03	3.791E-03	3.681E-03

**FIGURE 19** Infinite 3D plate with an elliptical hole. Symmetric boundary conditions are applied to plane YZ. Stress-free surface boundary conditions are applied to the boundary of the elliptical hole and to the top surface of the plate. The plate is fixed in the Z direction on the bottom surface of the plate. The displacement field of the exact solution is applied to the other boundaries of the domain**TABLE 2** Results in terms of L_2 relative error norm for the problem of an infinite 3D plate with an elliptical hole

Parameter	Coarse model(34,038 nodes)		Fine model(168,116 nodes)	
	w/o visibility criterion	w/ visibility criterion	w/o visibility criterion	w/ visibility criterion
σ_{11}	7.112E+00	1.087E+00	5.887E+00	2.280E-01
σ_{12}	8.995E+00	2.095E+00	5.515E+00	6.252E-01
σ_{22}	4.722E+00	9.264E-01	4.818E+00	3.459E-01
σ_{VM}	1.073E+01	1.650E+00	9.752E+00	5.179E-01

3D L-shape

The model of a 3D L-shape in mode I loading is presented in Figure 20. The solution to this problem is presented in Section 3.4.1 for the 2D case. Stress-free boundary conditions are applied to the inner surface of the “L.” The bottom and top surfaces of the body are fixed in the Z direction. The displacement field of the exact solution is applied to the other boundaries of the domain.

The L_2 relative error norm is presented in Table 3 for the σ_{11} , σ_{12} , σ_{22} , and σ_{33} stress components and for the von Mises stress σ_{VM} . The results for the stress components σ_{13} and σ_{23} are not presented as the stresses are null for these components.

3.5.2 | Results

The results for the problem of an infinite body with a spherical cavity are presented in Table 1. We can see from these results that only a slight error reduction is observed when the visibility criterion is used. A small error increase is observed for the σ_{13} stress component for the coarse model. The error is reduced by a factor of 3 approximately, between the coarse and the fine model.

FIGURE 20 3D L-shape. Stress-free boundary conditions are applied to the inner surface of the “L.” The bottom and top surfaces of the body are fixed in the Z direction. The displacement field of the exact solution is applied to the other boundaries of the domain

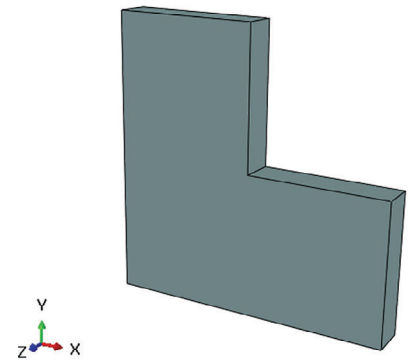


TABLE 3 Results in terms of L_2 relative error norm for the 3D L-shape problem

Parameter	Coarse model (28,890 nodes)		Fine model (119,683 nodes)	
	w/o visibility criterion	w/ visibility criterion	w/o visibility criterion	w/ visibility criterion
σ_{11}	6.109E+00	1.943E-01	6.762E-01	1.579E-01
σ_{12}	5.039E+00	2.082E-01	4.937E-01	1.284E-01
σ_{22}	4.527E+00	2.035E-01	6.383E-01	1.479E-01
σ_{33}	1.484E+01	3.445E-01	2.091E+00	3.138E-01
σ_{VM}	9.410E+00	2.514E-01	9.263E-01	1.596E-01

The results obtained for the infinite body with a spherical cavity are similar to the results obtained for the 2D cylinder. The use of the visibility criterion, in conjunction with a threshold angle of 5.0° , does not lead to an important decrease or increase of the error. With such a threshold angle, the selected collocation stencils are very close with and without consideration of the visibility criterion.

The results for the problem of an infinite 3D plate with an elliptical hole are presented in Table 2. We can see from these results that an important error reduction is achieved when the visibility criterion is used. The error is reduced by a factor of 6 approximately, for the coarse model and by a factor 19 for the fine model. The error is reduced by a factor of 3 approximately, between the coarse and the fine model, when the visibility criterion is used.

As expected, these results are similar to the ones obtained for the 2D plate. In the areas of the model where the concavity is of high curvature, the visibility criterion allows capturing more accurately the geometry of the model.

The results for the 3D L-shape problem are presented in Table 3. We can see from these results that an important error reduction is achieved when the visibility criterion is used. The error is approximately reduced by a factor 37 for the coarse model and by a factor 6 for the fine model. The error is reduced by a factor nearing 1.6 between the coarse and the fine model when the visibility criterion is used.

3.6 | Discussion

The results obtained for the 3D problems are consistent with those obtained for the 2D problems. A significant error reduction is observed for the infinite plate with an elliptical hole and for the L-shape problem, both in 2D and in 3D, when the visibility criterion is considered. As expected, the error reduction is more significant for the L-shape problem due to the presence of a sharp corner.

For the case of an infinite plate with an elliptical hole (2D and 3D) and for the infinite body with a spherical cavity problem, the error reduction achieved when the visibility criterion is used tends to decrease as the number of nodes in the domain and on the boundaries of the domain increases. This result is expected as the angle between two adjacent surface elements decreases for these problems when the node density increases. This result is not observed for the 2D L-shape problem as the angle between surface elements on each side of the singularity is not affected by the discretization. For the 3D L-shape, the error reduction achieved when the visibility criterion is used is smaller for the fine model than for the coarse model. This is attributed to the important error observed for the coarse model without consideration of the visibility criterion.

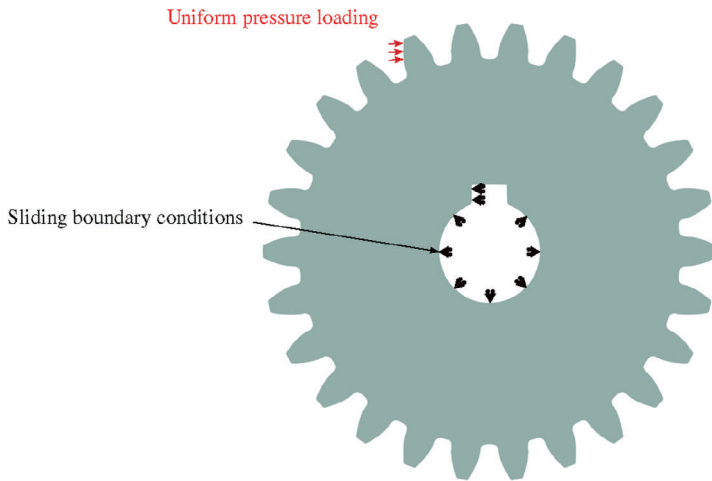


FIGURE 21 Boundary conditions applied to model a gear coupled to a shaft by a key

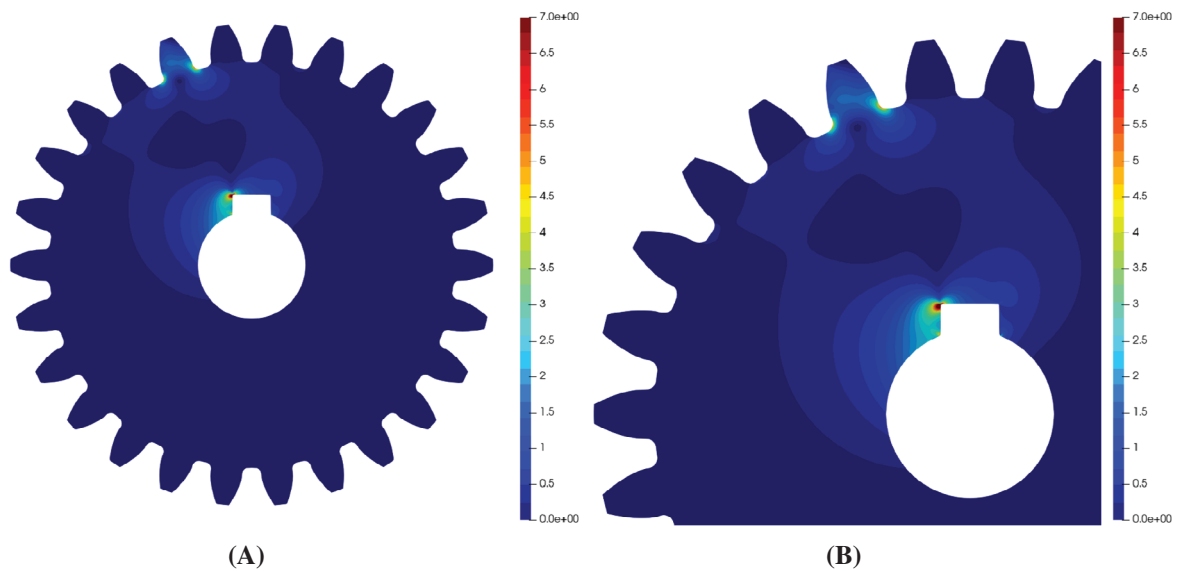


FIGURE 22 Gear coupled to a shaft—Solution in terms of von Mises stress obtained from a finite element model composed of 132,665 nodes and 262,193 linear triangular elements. The results are shown for the stress range 0–7 for comparison purpose

For the 2D cylinder under internal pressure, the results are only slightly affected by the use of the visibility criterion if a threshold angle of 1.0° or 5.0° is used. A threshold angle of 5.0° leads to the smallest error. For the infinite plate with an elliptical hole and for the 2D L-shape problems, threshold angles of 1.0° and 5.0° lead to significant error reductions. Based on these results, we believe that the selection of a threshold angle of 5.0° is a reasonable choice for most problems.

The problems presented in the previous section were used to benchmark the proposed method against exact solutions to determine the most suitable threshold parameter. To confirm the suitability of the approach to engineering problems, we applied the method to a more complex problem: the loading of a gear coupled to a shaft by a key. The problem is approximated by a 2D plane stress model presented in Figure 21. Very small radii were modeled at the corners of the keyway. We modeled the coupling between the shaft and the gear by a sliding boundary condition between the gear and the shaft and between the gear and the key. We applied a uniform pressure loading on a face of a tooth. We compared the results in terms of von Mises stress from a coarse discretization (33,404 nodes) and a fine discretization (109,858 nodes) with and without use of the visibility criterion. A visibility threshold of 5.0° is selected. The results are compared to results obtained from a very fine finite element model composed of 132,665 nodes and 262,193 linear triangular elements. The finite element problem is solved with the code *aster*.⁴⁶

The results in terms of von Mises stress from the finite element model are presented in Figure 22. The results show an important stress concentration at the left corner of the keyway. The fillets on each side of the loaded tooth are also subject to a stress concentration but of a much lower magnitude. The results in terms of von Mises stress obtained from

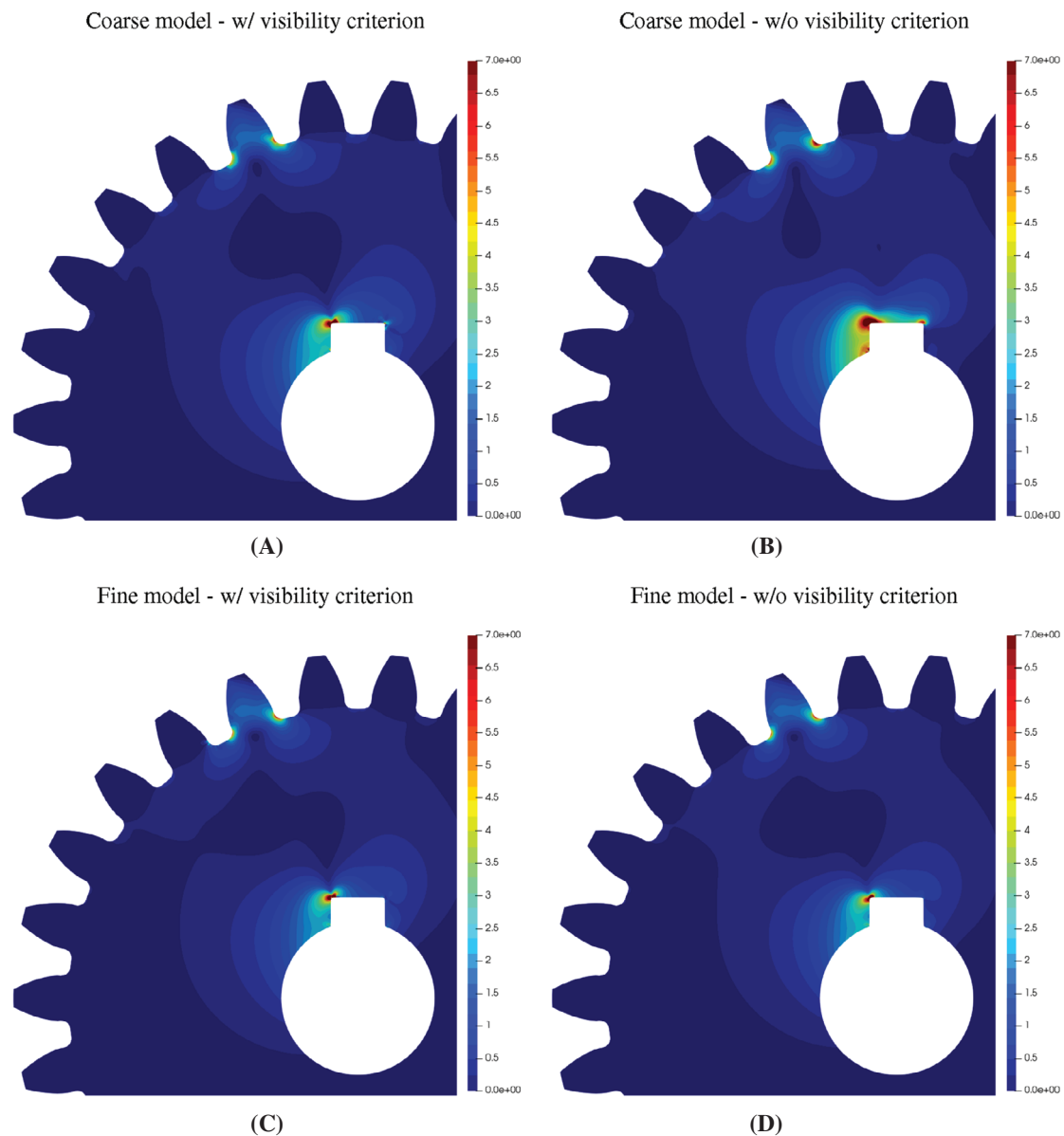


FIGURE 23 Gear coupled to a shaft—Solution in terms of von Mises stress from collocation with and without use of the visibility criterion for coarse (33,404 nodes) and fine (109,858 nodes) models. The results are shown for the stress range 0–7 for comparison purpose

the collocation models are presented in Figure 23. For the coarse model, the results obtained with the visibility criterion are very close to the results obtained from the finite element model. The zone of high stress concentration obtained from the model without consideration of the visibility criterion is more important. This is understood by the less accurate representation of the geometry in the vicinity of the corners of the keyway. For the fine model, little difference can be observed between the collocation results with and without consideration of the visibility criterion. This result is similar to what was observed from the results presented in Sections 3.4.2 and 3.5.2.

4 | USE OF THE ALGORITHM FOR MODEL REFINEMENT

The purpose of the algorithm presented in Section 2 is to assess if a potential support node is “visible” from a collocation node (i.e., to assess if the segment connecting a collocation node to a support node intersects the boundary of the domain with an angle smaller than a defined threshold). The algorithm can also be used to assess if a node is located inside or outside a given domain.

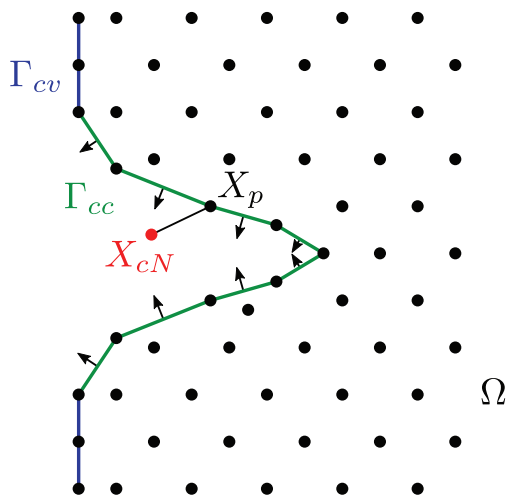


FIGURE 24 Assessment of the location of the potential new collocation node X_{cN} with respect to the domain Ω

In the context of model refinement, additional nodes are added to the domain. Algorithm #2 presented in Figure 3 can be used to assess if a node is located inside or outside a given domain. The nodes added to the model can be considered as new collocation nodes noted X_{cN} (see Figure 24). For each added node, a k-d tree is used to locate the closest node. Depending on the regularity of the model, more than one node can be considered. If the segment connecting X_{cN} to X_p is considered as intersecting the boundary based on the condition stated in Algorithms #3 and #4 then the new collocation node is not in the domain. Note that depending on the refinement method, boundary elements might be needed over the whole domain and not only along the convex boundaries as for the visibility criterion algorithm.

5 | CONCLUSION

The algorithm presented in Section 2 allows the selection of the support nodes of each collocation node of a domain based on the visibility criterion. We showed in Section 2.2 that a threshold angle allows a more robust node selection for any concave and singular problem. We selected a threshold angle of 5.0° as it led for the considered problems to an error reduction. Relatively simple problems were used to benchmark our results against exact solutions. More complex geometries may comprise concavities of high or low curvature, relatively to the node spacing, or singularities. For these three cases, we showed that the use of the visibility criterion, in conjunction with a threshold angle of 5.0° , leads to a reduction of the error or does not affect the solution for problems having concavities of low curvature. We also showed for the model of a gear coupled to a shaft by a key that the use of the visibility criterion leads to a stress field closer to one obtained from a very fine finite element model. Therefore, we recommend that a threshold angle of 5.0° be used as a starting point for most problems. The selected threshold can then be adjusted if needed.

Based on the algorithm presented in this article, one can readily assess a new convex, concave, or singular geometry, using a collocation method. The error is minimized in the concave areas of the domain by the use of the visibility criterion.

To enhance the reliability of the solution, a posteriori error estimators can be used to determine the areas where the error is the greatest. New nodes can be placed in these areas in order to reduce the estimated error. The algorithm presented in this article can be used to ensure that the added nodes remain inside of the domain.


ACKNOWLEDGMENTS

The authors are grateful for the funding from the Luxembourg National Research Fund (INTER/FWO/15/10318764) and the funding for the DRIVEN project from the European Union's Horizon 2020 research and innovation program (grant agreement No 811099).

DATA AVAILABILITY STATEMENT

The data that support the findings of this study are openly available in <https://gitlab.com/tjacquemin/collocation-visibility>.

ORCID

Stéphane P. A. Bordas  <https://orcid.org/0000-0001-7622-2193>

REFERENCES

1. Runge C. Über eine Methode die partielle Differentialgleichung $\Delta u = \text{constants}$ numerisch zu integrieren. *Z Math Phys.* 1908;56:225-232.
2. Jacquemin T, Tomar S, Agathos K, Mohseni-Mofidi S, Bordas S. Taylor-series expansion based numerical methods: a primer, performance benchmarking and new approaches for problems with non-smooth solutions. *Arch Comput Methods Eng.* 2019;27:1465-1513. <https://doi.org/10.1007/s11831-019-09357-5>.
3. Monaghan J. Smoothed particle hydrodynamics. *Annu Rev Astron Astrophys.* 1992;30(1):543-574. <https://doi.org/10.1146/annurev.aa.30.090192.002551>.
4. Liu WK, Jun S, Zhang YF. Reproducing kernel particle methods. *Int J Numer Methods Fluids.* 1995;20(8-9):1081-1106. <https://doi.org/10.1002/flid.1650200824>.
5. Shepard D. *A Two-Dimensional Interpolation Function for Irregularly-Spaced Data*. United States: ACM Press; 1968.
6. Lancaster P, Salkauskas K. Surfaces generated by moving least squares methods. *Math Comput.* 1981;37(155):141-141. <https://doi.org/10.1090/s0025-5718-1981-0616367-1>.
7. Oñate E, Idelsohn S, Zienkiewicz O, Taylor R. A finite point method in computational mechanics. application to convective transport and fluid flow. *Int J Numer Methods Eng.* 1996;39(22):3839-3866. [https://doi.org/10.1002/\(sici\)1097-0207\(19961130\)39:22<3839::aid-nme27>3.0.co;2-r](https://doi.org/10.1002/(sici)1097-0207(19961130)39:22<3839::aid-nme27>3.0.co;2-r).
8. Macneal R. An asymmetrical finite difference network. *Q Appl Math.* 1953;11(3):295-310.
9. Forsythe G, Wasow W. *Finite Difference Methods for Partial Differential Equations*. United Kingdom: Wiley; 1960.
10. Jensen P. Finite difference techniques for variable grids. *Comput Struct.* 1972;2(1-2):17-29. [https://doi.org/10.1016/0045-7949\(72\)90020-x](https://doi.org/10.1016/0045-7949(72)90020-x).
11. Perrone N, Kao R. A general finite difference method for arbitrary meshes. *Comput Struct.* 1975;5(1):45-57. [https://doi.org/10.1016/0045-7949\(75\)90018-8](https://doi.org/10.1016/0045-7949(75)90018-8).
12. Liszka T, Orkisz J. The finite difference method at arbitrary irregular grids and its application in applied mechanics. *Comput Struct.* 1980;11(1-2):83-95. [https://doi.org/10.1016/0045-7949\(80\)90149-2](https://doi.org/10.1016/0045-7949(80)90149-2).
13. Orkisz J. *Finite Difference Method (Part III)*. New York, NY: Springer-Verlag; 1998:335-432.
14. Belytschko T, Lu Y, Gu L. Element-free Galerkin methods. *Int J Numer Methods Eng.* 1994;37(2):229-256. <https://doi.org/10.1002/nme.1620370205>.
15. Duflo M. *Application des méthodes sans maillage en mécanique de la rupture* [PhD thesis]. Université de Liege; 2004.
16. Nguyen VP, Rabczuk T, Bordas S, Duflo M. Meshless methods: a review and computer implementation aspects. *Math Comput Simul.* 2008;79(3):763-813. <https://doi.org/10.1016/j.matcom.2008.01.003>.
17. Taleei A, Dehghan M. An efficient meshfree point collocation moving least squares method to solve the interface problems with nonhomogeneous jump conditions. *Numer Methods Partial Differ Equ.* 2014;31(4):1031-1053. <https://doi.org/10.1002/num.21935>.
18. Lee SH, Yoon YC. Meshfree point collocation method for elasticity and crack problems. *Int J Numer Methods Eng.* 2004;61(1):22-48. <https://doi.org/10.1002/nme.1053>.
19. Lee SH, Kim KH, Yoon YC. Particle difference method for dynamic crack propagation. *Int J Impact Eng.* 2016;87:132-145. <https://doi.org/10.1016/j.ijimpeng.2015.06.001>.
20. Organ D, Fleming M, Terry T, Belytschko T. Continuous meshless approximations for nonconvex bodies by diffraction and transparency. *Comput Mech.* 1996;18(3):225-235. <https://doi.org/10.1007/bf00369940>.
21. Zhuang X, Augarde C, Bordas S. Accurate fracture modelling using meshless methods, the visibility criterion and level sets: formulation and 2D modelling. *Int J Numer Methods Eng.* 2011;86(2):249-268. <https://doi.org/10.1002/nme.3063>.
22. Sukumar N, Moran B, Black T, Belytschko T. An element-free Galerkin method for three-dimensional fracture mechanics. *Comput Mech.* 1997;20(1-2):170-175. <https://doi.org/10.1007/s004660050235>.
23. Duflo M, Nguyen-Dang H. A meshless method with enriched weight functions for fatigue crack growth. *Int J Numer Methods Eng.* 2004;59(14):1945-1961. <https://doi.org/10.1002/nme.948>.
24. Fleming M, Chu Y, Moran B, Belytschko T. Enriched element-free Galerkin methods for crack tip fields. *Int J Numer Methods Eng.* 1997;40(8):1483-1504. [https://doi.org/10.1002/\(sici\)1097-0207\(19970430\)40:8<1483::aid-nme123>3.0.co;2-6](https://doi.org/10.1002/(sici)1097-0207(19970430)40:8<1483::aid-nme123>3.0.co;2-6).
25. Rabczuk T, Belytschko T. Adaptivity for structured meshfree particle methods in 2D and 3D. *Int J Numer Methods Eng.* 2005;63(11):1559-1582. <https://doi.org/10.1002/nme.1326>.
26. Zhuang X, Augarde C, Mathisen K. Fracture modeling using meshless methods and level sets in 3D: framework and modeling. *Int J Numer Methods Eng.* 2012;92(11):969-998. <https://doi.org/10.1002/nme.4365>.
27. Rabczuk T, Belytschko T. Cracking particles: a simplified meshfree method for arbitrary evolving cracks. *Int J Numer Methods Eng.* 2004;61(13):2316-2343. <https://doi.org/10.1002/nme.1151>.
28. Rabczuk T, Song JH, Belytschko T. Simulations of instability in dynamic fracture by the cracking particles method. *Eng Fract Mech.* 2009;76(6):730-741. <https://doi.org/10.1016/j.engfracmech.2008.06.002>.
29. Rabczuk T, Zi G, Bordas S, Nguyen-Xuan H. A simple and robust three-dimensional cracking-particle method without enrichment. *Comput Methods Appl Mech Eng.* 2010;199(37-40):2437-2455. <https://doi.org/10.1016/j.cma.2010.03.031>.
30. Shimrat M. Algorithm 112: position of point relative to polygon. *Commun ACM.* 1962;5(8):434. <https://doi.org/10.1145/368637.368653>.
31. Chinn W, Steenrod N. *First Concepts of Topology*. United States: The Mathematical Association of America; 1966.

32. O'Rourke J. *Computational Geometry in C (Cambridge Tracts in Theoretical Computer Science (Paperback))*. 2nd ed. Cambridge, MA: Cambridge University Press; 1998.
33. Möller T, Trumbore B. Fast, minimum storage ray-triangle intersection. *J Graph Tools*. 1997;2(1):21-28. <https://doi.org/10.1080/10867651.1997.10487468>.
34. Alliez P, Tayeb S, Wormser C. *3D Fast Intersection and Distance Computation*. 5.0. CGAL Editorial Board; 2019.
35. Schönauer W. Generation of difference and error formulae of arbitrary consistency order on an unstructured grid. *ZAMM J Appl Math Mech / Zeitschrift für Angewandte Mathematik und Mechanik*. 1998;78(S3):1061-1062. <https://doi.org/10.1002/zamm.19980781599>.
36. Kennett D, Timme S, Angulo J, Badcock K. Semi-meshless stencil selection for anisotropic point distributions. *Int J Comput Fluid Dyn*. 2012;26(9-10):463-487. <https://doi.org/10.1080/10618562.2012.744450>.
37. Seibold B. Minimal positive stencils in meshfree finite difference methods for the Poisson equation. *Comput Methods Appl Mech Eng*. 2008;198(3-4):592-601. <https://doi.org/10.1016/j.cma.2008.09.001>.
38. Davydov O, Oanh DT. Adaptive meshless centres and RBF stencils for Poisson equation. *J Comput Phys*. 2011;230(2):287-304. <https://doi.org/10.1016/j.jcp.2010.09.005>.
39. Davydov O, Oanh DT, Tuong NM. Octant-based stencil selection for meshless finite difference methods in 3D. *Vietnam J Math*. 2019;48(1):93-106. <https://doi.org/10.1007/s10013-019-00364-4>.
40. Geuzaine C, Remacle JF. Gmsh: a 3-D finite element mesh generator with built-in pre- and post-processing facilities. *Int J Numer Methods Eng*. 2009;79(11):1309-1331. <https://doi.org/10.1002/nme.2579>.
41. Gao XL. A general solution of an infinite elastic plate with an elliptic hole under biaxial loading. *Int J Press Vessel Pip*. 1996;67(1):95-104. [https://doi.org/10.1016/0308-0161\(94\)00173-1](https://doi.org/10.1016/0308-0161(94)00173-1).
42. Babuška I, Suri M. The h-p version of the finite element method with quasiuniform meshes. *ESAIM Math Model Numer Anal*. 1987;21(2):199-238. <https://doi.org/10.1051/m2an/1987210201991>.
43. Ainsworth M, Senior B. Aspects of an adaptive hp-finite element method: adaptive strategy, conforming approximation and efficient solvers. *Comput Methods Appl Mech Eng*. 1997;150(1-4):65-87. [https://doi.org/10.1016/s0045-7825\(97\)00101-1](https://doi.org/10.1016/s0045-7825(97)00101-1).
44. Li Z, Lim C, He L. Stress concentration around a nano-scale spherical cavity in elastic media: effect of surface stress. *Eur J Mech A Solids*. 2006;25(2):260-270. <https://doi.org/10.1016/j.euromechsol.2005.09.005>.
45. Sharma R, Zhang J, Langelaar M, van Keulen F, Aragón AM. An improved stress recovery technique for low-order 3D finite elements. *Int J Numer Methods Eng*. 2018;114(1):88-103. <https://doi.org/10.1002/nme.5734>.
46. Electricité de France. Finite element code_aster analysis of structures and thermomechanics for studies and research; 1989. Open source on www.code-aster.org

How to cite this article: Jacquemin T, Bordas SPA. A unified algorithm for the selection of collocation stencils for convex, concave, and singular problems. *Int J Numer Methods Eng*. 2021;122:4292–4312. <https://doi.org/10.1002/nme.6703>